Available online at www.sciencedirect.com
ScienceDirect
Cement and Concrete Research 36 (2006) 1643–1652
Cement and Concrete Research

Restraining effects of fibers during non-uniform drying of cement composites

Zhen Li [a], Miguel A. Perez Lara [b], J.E. Bolander [a,*]

[a] Department Civil and Environmental Engng., Univ. of California, Davis, CA 95616-5294, USA
[b] Dept. Civil Engineering, Universidad Autonoma de Querétaro, Mexico

Received 19 October 2005; accepted 10 April 2006

Abstract

Fiber reinforcement is often added to concrete materials to reduce shrinkage strains due to drying of the cement-based matrix and the associated potential for crack growth. The role of fibers in restraining shrinkage is complicated due to their semi-random distribution within the material, non-uniform drying of the cement-based matrix phase, and the three-dimensional geometry and boundary conditions of the structural component. This work describes an irregular lattice approach for explicitly modeling individual fibers, and their collective actions, within fiber reinforced cement composites (FRCC) subjected to drying environments. The spatial and orientation distributions of the fibers conform to the structural boundaries and could account for other aspects of the production process. The stresses in the fibers differ greatly depending on whether uniform or non-uniform drying is considered, the latter case being more realistic. Whereas the emphasis is on modeling the pre-cracking actions of the fibers, this paper briefly discusses the potential for using this discrete type of approach to model fracture of FRCC.

Keywords: Drying; Diffusion; Shrinkage; Fiber reinforcement; Modeling

1. Introduction

Cement based composites exhibit various forms of shrinkage due to the transport and consumption of moisture over time, with the greatest amount of shrinkage produced during early ages of the composite. Such shrinkage strains are often problematic in that they produce tensile stresses that can be sufficiently large to crack the material. Stresses may be generated due to external restraints on the structural member, internal restraints due to the presence of stiff inclusions (e.g. aggregates, reinforcement) and non-uniform moisture movement within the member. Other load sources, such as thermal gradients due to heat of hydration and environmental effects (e.g. solar heating and nighttime cooling), generate stress within the material and may also contribute to crack development. Such early age cracking can seriously compromise the durability of concrete structures subjected to severe environments [1].

Discrete fiber reinforcement has been used in cement composites to reduce crack widths and toughen the cracked composite under various types of loading [2–4]. One of the primary applications of fiber reinforcement is in reducing or eliminating the effects of several forms of shrinkage cracking. Low modulus synthetic fibers have been useful in reducing plastic shrinkage cracking at young ages, prior to significant hardening of the cement-based matrix [5–7]. At later ages, the presence of stiff fibers (e.g. steel fibers) helps restrain shrinkage due to drying of the cement-based matrix [8,9]. Whereas conceptual models have been developed to explain the role of fibers in restraining shrinkage strain, direct quantitative links between the individual fibers and global behavior have been lacking. Reasons for this include: 1) the complexity of the three-dimensional processes of moisture movement and matrix aging at early ages; 2) the presence of various forms of internal and external constraint acting on the material; and 3) the semi-random arrangement of the fibers within the three-dimensional material domain.

This paper presents a numerical model of fiber reinforced cement composites (FRCC) and its application to studying the role of fibers during material drying. The simulations are based on an irregular lattice model of both the cement-based matrix phase, which is assumed to be homogeneous, and the fiber

* Corresponding author. Fax: +1 530 752 7872.
E-mail address: jebolander@ucdavis.edu (J.E. Bolander).

0008-8846/$ - see front matter © 2006 Elsevier Ltd. All rights reserved.
doi:10.1016/j.cemconres.2006.04.001

inclusions. The various forms of restraint, mentioned above, are naturally included in the model. The simulation results are compared with those of an analytical model and experimental data. Due to the explicit modeling of each fiber, the variation of stress in each fiber is obtained. Few studies have explicitly modeled multiple individual fibers within cement composites [10–12] and those that do have focused primarily on the effects of external loading. Comparing the response of individual fibers, and their collective behavior, during uniform and non-uniform shrinkage of the cement-based matrix material is one primary objective of this work. Whereas the emphasis is on modeling the pre-cracking actions of the fibers, this paper briefly discusses the potential for using this discrete type of approach to model fracture of FRCC.

2. Research significance

A general framework is developed for studying individual fibers, and their collective behavior, within FRCC subjected to drying. The simulations provide insight into the mechanisms by which fibers restrain material shrinkage, with particular attention to the differences between uniform and non-uniform drying of the matrix material. The explicit modeling of individual fibers provides a level of inspection not attainable with macro-models that smear the effects of fibers over the material volume and enables the study of fiber distribution and orientation effects, as might be induced by the production processes. With appropriate modifications, the FRCC model described in this paper could serve as a basis for studying the role of irregular fiber distributions in crack formation and propagation, including the effects of cracking and fiber pullout from the matrix phase.

3. Simulation framework

Lattice models have been used to study various aspects of concrete materials [13–16]. In this paper, a three-dimensional lattice is used to model moisture diffusion and its coupling to strain and stress production in cement-based materials. The lattice topology is defined by the Delaunay tessellation [17] of an irregular set of nodal points, whereas the lattice element properties scale according to the dual Voronoi tessellation of the same set of nodes, as described below. The Delaunay and Voronoi tessellations of a rectangular prism of material are shown in Fig. 1. The lattice nodes are used to represent both the scalar field of pore humidity and the vector field of generalized displacements. The lattice approach accommodates a semi-discrete modeling of short fiber reinforcement, which accounts for the distribution and orientation of individual fibers within the material volume.

3.1. Lattice model of moisture diffusion

3.1.1. Model formulation

The general approach for modeling moisture diffusion in cement composites, the convective boundary conditions at exposed surfaces, and the coupling of the diffusion and strain

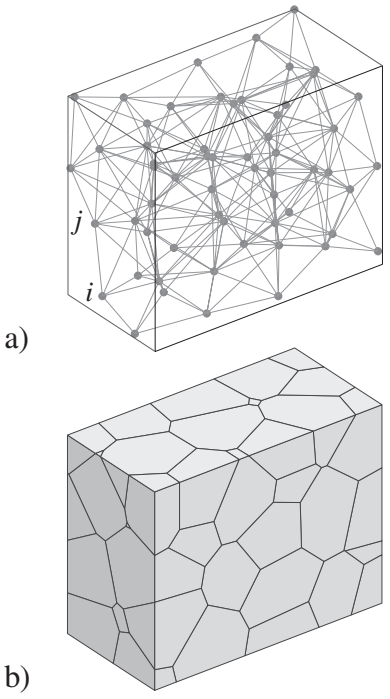

Fig. 1. Domain discretization for coupled moisture diffusion and elasticity analyses: a) Delaunay tessellation; and b) Voronoi tessellation.

analyses, are based on the works of Bazant and Najjar [18] and Martinola and Wittmann [19]. For isothermal conditions, with no sinks or sources present, the governing equation for transient nonlinear diffusion problems is

$$\frac{\partial H}{\partial t} = \mathrm{div}[D(H)\mathrm{grad}H] \tag{1}$$

where H is the pore relative humidity and $D(H)$ is a humidity dependent diffusion coefficient, which is a scalar quantity for isotropic conditions.

Each edge ij of the Delaunay tessellation can be viewed as a conduit element [14] that transports moisture between nodes i and j (Fig. 1). The semi-discrete form of Eq. (1) is

$$\mathbf{M}\dot{\mathbf{H}} + \mathbf{K}\mathbf{H} = \mathbf{f} \tag{2}$$

where $\mathbf{H}$ is the vector of nodal relative humidities and the dot over $\mathbf{H}$ indicates time derivative. The system matrices, $\mathbf{M}$ and $\mathbf{K}$, are assembled from the elemental capacity and diffusivity matrices, respectively.

$$\mathbf{M}_e = \frac{h_{ij}A_{ij}}{6d}\begin{bmatrix} 2 & 1 \\ 1 & 2 \end{bmatrix} \tag{3}$$

$$\mathbf{K}_e = \frac{DA_{ij}}{h_{ij}}\begin{bmatrix} 1 & -1 \\ -1 & 1 \end{bmatrix} \tag{4}$$

as would be done for the finite element analysis of potential flow problems using two-node elements [20]. Element length h_{ij} is the distance between nodes i and j; cross-section area A_{ij} is set equal to the area of the Voronoi facet corresponding to the same two nodes. In the elemental capacity matrix, $d = 1.0$, 2.0, and 3.0 for 1-d, 2-d, and 3-d networks, respectively. A Crank–Nicolson

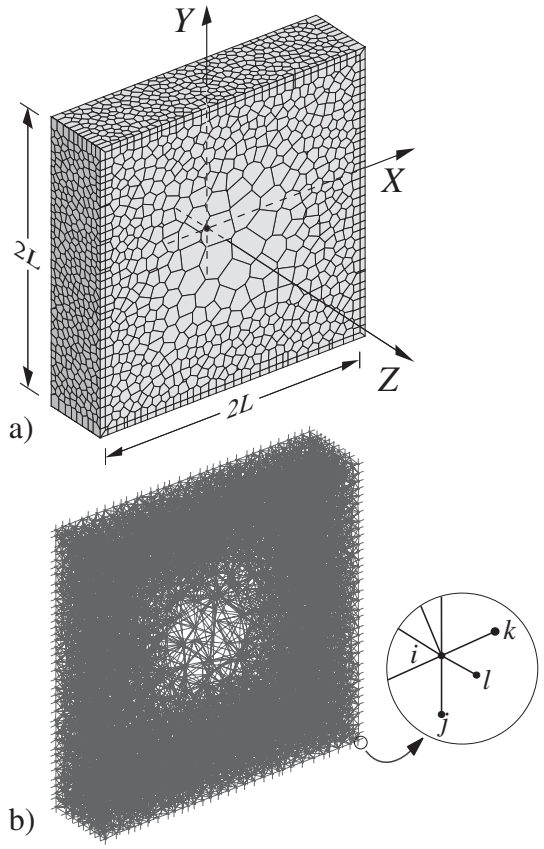

Fig. 2. Model set-up for prismatic section under drying: a) Voronoi discretization; b) conduit network and boundary details.

scheme is used to solve the diffusion equations [21], along with iterations that account for the dependence of the diffusion coefficient on H, which is given as

$$D(H) = \beta \exp(\gamma H) \tag{5}$$

where β and γ are parameters that can be determined by calibration with experimental results [19]. Eqs. (1) and (2) model moisture transport in a macroscopic sense and D should be regarded as an apparent moisture diffusion coefficient, representing complex processes and dependencies on the material constituents [22]. Moisture exchange between the material boundary and the atmosphere is modeled using convective boundary conditions of the form

$$q_s = C_F(H_s - H_a) \tag{6}$$

where q_s is moisture flux across the boundary, H_s and H_a are the relative humidities at the material surface and in the surrounding atmosphere, respectively, and C_F is the film coefficient.

3.1.2. Model verification: drying of a uniform half-space

The drying of a square prism (of dimensions $2L \times 2L \times \alpha L$) is used to verify the diffusion model for the case of constant diffusivity. If α is large, end effects are not significant when analyzing the moisture movement in an interior region of the prism. For such a case, moisture movement should be perpendicular to the longitudinal prism axis, so that typical behavior can be simulated using one slice of the domain (Fig. 2). To provide smoother contours of humidity potential, a finer mesh is used near the surface where the humidity gradients are larger. The inset picture in Fig. 2b shows details of the conduit network at a typical corner, where lattice elements $\overline{ij}$ and $\overline{ik}$ represent the convective boundary condition at the interface between prism surface and the drying environment. For the example that follows, the drying environment is maintained at a relative humidity $H_a = 0.5$; the relative humidity of all prism nodes are initialized to $H_0 = 1.0$. The film coefficient in Eq. (6) is given a large value so that $H_s \approx H_a$ throughout the course of the analysis. Element $\overline{il}$ represents the zero-flux boundary condition, $q_s = 0$. Other surface layer elements, visible as part of the mesh (Fig. 2), are handled in a similar manner.

The results of the simulation are given in Fig. 3, which shows moisture contour plots for the cross section $Z = 0$ after various periods of drying. Time is expressed in terms of $\hat{t}$, corresponding to the time at which the humidity along the section centerline, $X = 0$, is effectively less than H_0 (i.e. $H = H_0 - \delta$) where δ is a small number.) Without affecting the validity of the comparison, $\delta = 0.001$ was arbitrarily set to define $\hat{t}$. The moisture potentials of all nodes in the region ($X \geq 0$; $-L/20 \leq Y \leq L/20$) are plotted for the same periods of drying.

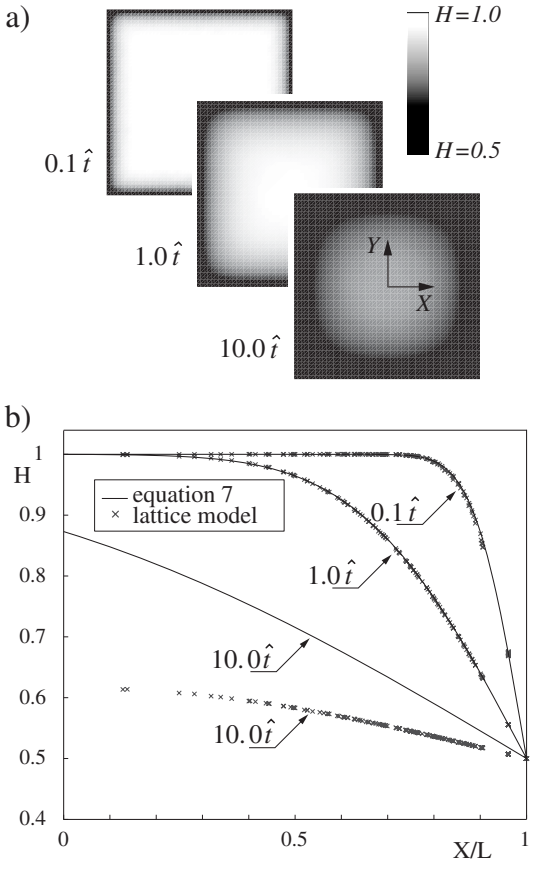

Fig. 3. a) Humidity contours; and b) humidity profiles after various periods of drying.

For comparison purposes, the figure also shows diffusion curves for a linear half-space [23], as given by:

$$H(x,t) = H_a + (H_0 - H_a)\mathrm{erf}\left[\frac{L-x}{2\sqrt{Dt}}\right] \quad (7)$$

where all values correspond to those used in the numerical simulation. For coarser meshes, similar good agreement between the model and theory is obtained, although the contours in Fig. 3a are not as smooth in appearance. For $t \gg \hat{t}$ the numerical solution noticeably differs from that of the theoretical half-space since the numerical model is effectively drying from more than one surface. The accuracy of the algorithms for nonlinear diffusion analysis has been verified through comparisons with results from commercial finite element software [24,25]. That work involved planar analyses of a cement composite overlay system subjected to drying.

3.2. Lattice model of matrix elasticity and shrinkage coupling

For the frame-type lattice elements used here, each lattice node has six degrees of freedom for modeling the elasticity of three-dimensional materials. The basic element is composed of a zero-size spring set, located at the area centroid (point *C*) of the Voronoi facet common to nodes *i* and *j*, and rigid arm constraints that link the spring set with the nodal degrees of freedom (Fig. 4). This approach is based on the rigid-body-spring concept of Kawai [26]. The spring set consists of three translational springs, oriented normal and tangential to the facet (Fig. 4b), and three rotational springs (not shown in the figure) about the same local axes. The uniaxial springs are assigned equal stiffness values:

$$k_n = k_s = k_t = E\frac{A_{ij}}{h_{ij}} \quad (8)$$

whereas the rotational springs are assigned stiffnesses:

$$k_{\phi n} = E\frac{J_p}{h_{ij}};\ k_{\phi s} = E\frac{I_{ss}}{h_{ij}};\ k_{\phi t} = E\frac{I_{tt}}{h_{ij}} \quad (9)$$

where E is the elastic modulus; J_p is the polar moment of inertia of the facet area; and I_{ss} and I_{tt} are the two principal moments of inertia of the facet area. The principal axes of the polygonal facet and its normal define the local n–s–t coordinate system shown in Fig. 4. For simplicity, the element local (x–y–z) axes are aligned in the same directions. The element stiffness matrix is constructed from these basic components, as described by Berton and Bolander [27]. The assignment of spring stiffness coefficients using Eqs. (8) and (9) (where h_{ij} and A_{ij} are defined by the Voronoi diagram) provides an elastically uniform lattice, i.e. a lattice that can reproduce uniform strain fields [24]. This condition of elastic uniformity is prerequisite to introducing heterogeneity, such as the fibers considered later in this paper.

In this paper, shrinkage strains in the elastic material arise from changes in relative humidity at the lattice nodes, as determined from the diffusion analyses described in Section 3.1. A constant hygral shrinkage coefficient, α_{sh}, is used in this coupling of the elasticity and diffusion analyses [19]

$$\Delta\varepsilon_S = \alpha_{sh}\Delta H \quad (10)$$

where ΔH is the difference in nodal relative humidity over the computational time step. Eq. (10) uses the average of ΔH calculated at the nodes of a given element and $\Delta\varepsilon_S$ is then introduced in the n (facet normal) direction of the corresponding element, which provides uniform volumetric straining of the lattice if ΔH is constant over the domain.

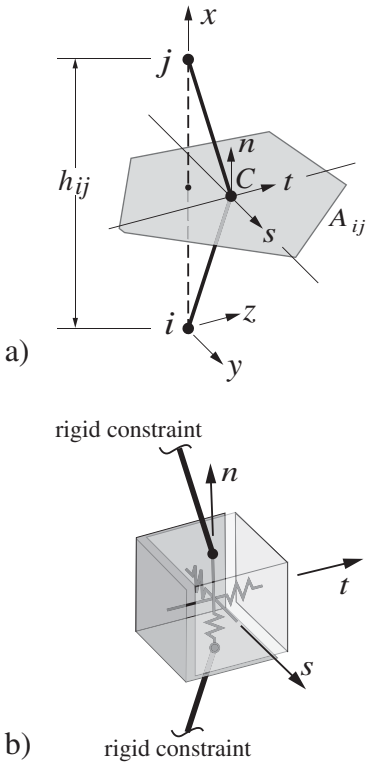

Fig. 4. a) Lattice element for modeling matrix material; b) view of zero-size spring set positioned at point *C*.

3.3. Semi-discrete modeling of fibers

A prescribed number (or volume fraction) of fibers is synthetically produced within the material domain. A pseudo-random number generator determines the coordinates of the fiber mid-point and the Euler angles for its orientation with respect to the global coordinate axes. Each fiber is represented as a semi-discrete entity within the composite material. The fiber model is now explained and then verified through an illustrative example.

3.3.1. Model formulation

A fiber lattice element is constructed for each intersection of the fiber with a Voronoi facet. For example, Fig. 5 depicts a single fiber passing through the Voronoi facet associated with nodes *i* and *j*. Element stiffness is derived from a zero-length spring located at point *P*, where the fiber intersects the facet. The

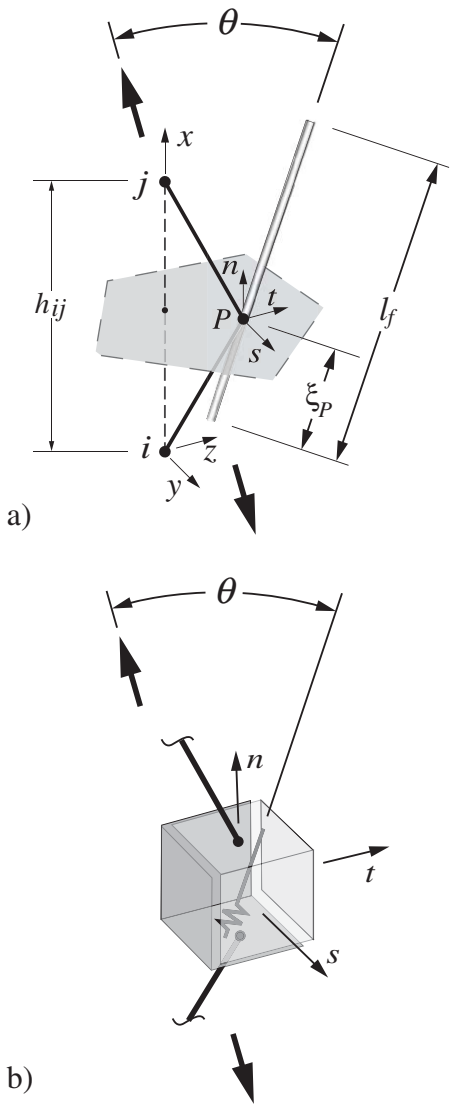

Fig. 5. a) Fiber lattice element *ij*; b) zero-length spring connecting rigid arms at point *P*.

spring is aligned in the fiber direction and assigned axial stiffness

$$k_f = \frac{A_f \sigma_f(\xi_P)}{(h_v/\cos\theta)\varepsilon_m} \tag{11}$$

where A_f=fiber cross-section area; θ=angle between the fiber axis and the direction of loading (Fig. 5); ε_m=matrix strain in the fiber direction; h_v is the distance between nodes *i* and *j* in the direction of loading; and $\sigma_f(\xi_P)$=fiber axial stress at the facet crossing, which is a distance ξ_P from the fiber end. The spring stiffness is transferred to the computational degrees of freedom defined at nodes *i* and *j* in a manner analogous to that of the matrix element formulation [27]. The fiber element acts in parallel with the matrix element associated with nodes *i* and *j* and therefore does not increase the number of degrees of freedom nor modify the sparsity of the system stiffness matrix of the lattice model. For this reason it is called a semi-discrete model of the fiber, in contrast to a discrete model of reinforcement presented elsewhere [28]. Using this semi-discrete approach, the typically large number of fibers present within actual macro-fiber composites can be modeled without significant computational burden.

This approach to modeling fibers is general in that any appropriate relation between $\sigma_f(\xi)$ and ε_m can be inserted within Eq. (11) to determine k_f. The expression used here, and illustrated in Fig. 6b, is based on a shear lag theory according to Cox [29]

$$\sigma_f(\xi) = E_f \varepsilon_m \left[1 - \frac{\cosh\left(\beta_1\left(\frac{l_f}{2} - \xi\right)\right)}{\cosh(\beta_1 l_f/2)}\right] \quad \text{for } 0 \le \xi \le l_f \tag{12}$$

where ξ=distance from the fiber end; E_f=fiber modulus of elasticity; l_f=fiber length; and β_1 depends on a number of factors including E_f, fiber radius, matrix shear modulus at the interface, fiber arrangement, and fiber volume fraction [30]. It is assumed that the fiber and matrix are elastic and no relative displacement occurs at the fiber–matrix interface. As explained elsewhere [10], k_f can be modified to account for the processes of interfacial debonding and frictional slip, which become active after cracks initiate within the matrix phase of the composite. It should be noted that creep processes would alter the fiber stresses over time. Basic creep of the bulk matrix material has been modeled using this lattice approach by

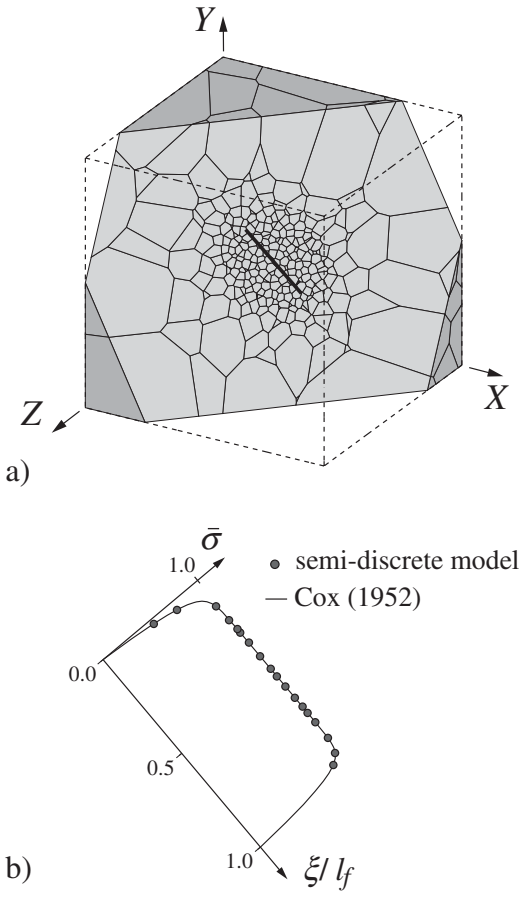

Fig. 6. a) Fiber embedded in matrix under uniaxial tension; and b) axial stress distribution along fiber length.

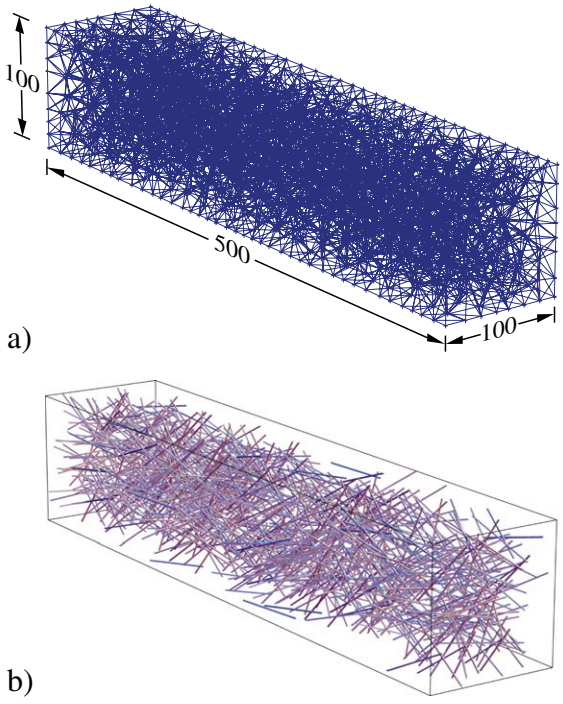

Fig. 7. Lattice model of shrinkage specimen: a) Delaunay discretization of material domain (dimensions in mm); and b) semi-random fiber distribution.

replacing each uniaxial spring in Fig. 4b with a number of Maxwell units that are connected in parallel [24]. In a similar way, creep local to each fiber could be modeled by considering viscoelasticity of the matrix and the matrix–fiber interface along the fiber length, especially near the fiber ends where stress transfer to the fiber is greatest. Additional model development is needed in this area.

3.3.2. Model verification: axial stress profile of a single fiber

Fig. 6a shows an exposed view of a single fiber embedded within a homogeneous matrix, which is subjected to uniform tensile strain ε_m in the X-direction. The fiber crosses multiple Voronoi facets so that a corresponding number of fiber elements are constructed. For a given fiber lattice element, axial stress in the element is obtained from $\sigma = F_f/A_f$, where F_f is the force in the corresponding zero-length spring (Fig. 5b). The modeling approach accurately represents length and orientation efficiency effects, as shown by the axial stress distributions along the fiber length given in Fig. 6b. Fiber axial stress has been normalized as follows:

$$\bar{\sigma} = \frac{\sigma}{E_f \varepsilon_m \cos^2\theta} \tag{13}$$

The solid circular marks indicate the stress level within each fiber lattice element (i.e. at each intersection of the fiber with a Voronoi facet).

The semi-discrete model matches theory since Cox's relation (Eq. (12)) is embedded in its spring element formulation and the fiber stiffness has been set small relative to the matrix stiffness terms, so that the strain field local to the fiber is not significantly modified by the presence of the fiber. The case where fiber stiffness is relatively large is examined in an example given later. Objectivity of the fiber model during matrix fracture, where fiber debonding and frictional pullout occur, has been demonstrated for the planar analysis of FRCC components [31].

4. Drying shrinkage of FRCC: numerical simulations

The numerical model is used to simulate the shrinkage behavior of FRCC specimens tested by Mangat and Azari [9]. In that experimental work, various fiber types and fiber volume fractions were placed within $500 \times 100 \times 100$ mm^3 test specimens made of either mortar or concrete. A three-dimensional discretization of this rectangular prism is shown in Fig. 7. The material parameters relevant to simulating the FRCC specimens are shown in Table 1. The assignment of parameter values for the moisture transport model is an area where additional work is needed; for this paper, these values were determined through computational inverse analysis. The concrete material is regarded as being homogeneous, so that the fiber inclusions are the only heterogeneous features. The effects of this assumption need to be studied in future work and, for that purpose, irregular lattice models of aggregate inclusions are being developed [32]. Results are also compared with those given by the micro-mechanical model of Zhang and Li [33], which is based on elastic shear lag theory and accounts for the random nature of the fiber distribution. Also, the time dependent variation of the elastic modulus of the mortar matrix is modeled as described in Ref. [33].

For this example, two different approaches are used to simulate drying shrinkage of the concrete materials: a) uniform shrinkage throughout the material domain, as prescribed by a code-type formula; and b) non-uniform shrinkage governed by a process of nonlinear moisture diffusion, as described in Section 3.1. In this manner, the behaviors of fibers during uniform and non-uniform shrinkage can be compared.

4.1. Uniform shrinkage case

The concrete is assumed to be homogeneous and shrink uniformly throughout the domain according to a code-type relation

$$\varepsilon_S(t) = \varepsilon_{SU}\left(\frac{t}{t+35}\right) \tag{14}$$

where ε_{SU} is the ultimate shrinkage strain and time t is measured in days after exposure to drying. Fig. 8 shows the shrinkage strains

Table 1
Material parameters used for numerical simulation (* indicates values set through back calculation)

Component	Parameter	Symbol	Value
Steel fiber	Elastic modulus	E_f	210 GPa
	Length	l_f	48.7 mm
	Diameter	d	1.14 mm
Matrix	Elastic modulus (at 28 days)	E_m	20 GPa
	Ultimate shrinkage strain of matrix	ε_{SU}	825 microstrain
	Hygral shrinkage coefficient*	α	0.00159/H
	Diffusion parameter (1)*	β	0.0112
	Diffusion parameter (2)*	γ	9.48
	Film coefficient*	C_f	0.59 mm/day

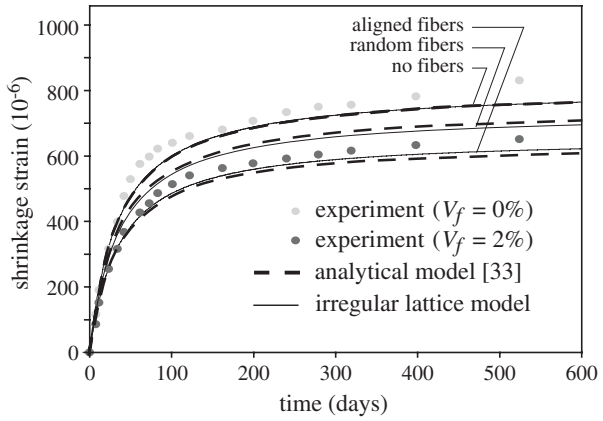

Fig. 8. Drying shrinkage strain as determined by experiments and modeling.

(measured over the specimen length) that develop over time in the material with no fibers and for a volume fraction of fibers V_f=2%. The shrinkage strain prescribed by Eq. (14) is introduced into each lattice element, resulting in uniform shrinkage throughout the domain when no fibers are present (due to elastic uniformity of the lattice, as noted in Section 3.2).

When fibers are included, the individual fibers restrict shrinkage of the concrete, which causes tension in the matrix and compression in the fibers. A similar effect results from the inclusion of stiff aggregates within the material, but the effect of aggregates is homogenized over the material volume in this work. The fiber distributions used for the lattice simulations are constrained by the specimen dimensions, so that there is directional alignment near the boundaries. The amount of shrinkage predicted for this quasi-random fiber composite is therefore slightly less than that given in reference [33], which assumed a uniformly at random distribution of fiber orientations. The model results agree fairly well with the experimental data, although the restraining effects of the fibers appear to be greater in the experiment. The effects of fiber orientation may partially account for this discrepancy, as explained in Section 4.4. Comparisons with other experimental results for the shrinkage of FRCC should also be made to better understand the numerical model in relation to actual behavior.

4.2. Non-uniform shrinkage case

At time t=0, the material domain is assumed to be saturated (i.e. H=1.0). All exposed surfaces are linked to an atmosphere with H=0.5 through convective boundary conditions, as expressed by Eq. (6). With increasing t, moisture flux occurs between the specimen surfaces and the atmosphere.

Humidity gradients provided by the moisture diffusion analysis lead to strain and stress development in the elastic model of the concrete specimen, according to Eq. (10). Prior to including fibers within the numerical model, the nonlinear diffusion parameters (presented in Table 1) were back-calculated to provide a macroscopic shrinkage curve close to that given by the uniform shrinkage model (Eq. (14)). The two curves are indistinguishable from one another in Fig. 9. Although the uniqueness of the back-calculated parameter values is an issue, the values are within the probable ranges for concrete materials. Furthermore, the magnitude of straining (and results of other simulations) indicates that some degree of diffuse cracking would be present in the specimen. However, the inclusion of fracture would imply an inverse fitting with various additional parameters related to the fracture processes, which is beyond the scope of this paper. Small, diffuse cracking would reduce the tensile stress in the surface layer of the material and, therefore, the driving force for the shrinkage, so that it would appear that the fibers are more effective in reducing the shrinkage.

In addition, the same diffusivity relations are used for the plain concrete and fiber reinforced concrete. Using Mercury Intrusion Porosimetry measurements, Wang et al. [7] show that the addition of fibers alters the size distribution and amount of pores in the cement-based matrix, effectively reducing water loss in the curing and drying processes of the cement paste. Decreasing the apparent diffusivity to account for fiber additions would reduce the amount of shrinkage strain, making it appear that the fibers were more effective in restraining shrinkage.

4.3. Fiber axial stress profiles

The interactions between fibers and the contracting matrix can be studied through plots of axial stress along each individual fiber length. A typical fiber crosses several cell boundaries and the stress in the fiber is computed at those locations (as shown for the single fiber in the example of Fig. 5b). Plotting these stress points for all fibers in one figure gives an overall indication of the interactions between the fibers and the matrix.

As the most basic case, a uniform triaxial strain is imposed on the lattice/fiber system, yielding the axial stress points shown in Fig. 10a, where ξ is the distance from the end of each fiber and ε_m is the strain in the matrix. (θ=0 in Eq. (13), since the shrinkage is assumed to be purely volumetric and therefore the same in each direction.) The stresses measured in the roughly 9000 fiber lattice elements agree precisely with Cox's theory.

In Fig. 10b, the fiber stress data is compared for the cases of uniform shrinkage of the matrix (Eq. (14)) and non-uniform

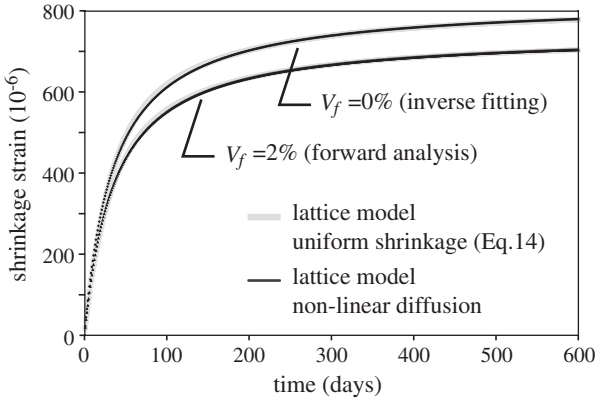

Fig. 9. Inverse fitting to determine drying shrinkage parameters and forward analysis with fiber inclusions.

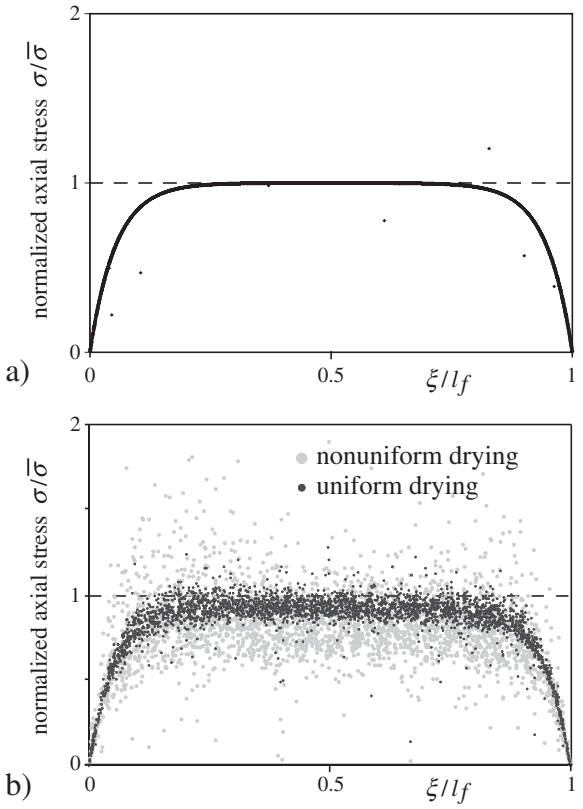

Fig. 10. Fiber axial stress profiles for $t=10$ days: a) imposed uniform shrinkage; and b) shrinkage due to uniform and non-uniform drying.

shrinkage due to moisture diffusion. Due to the restraining effects of fibers, both distributions of stress points appear, on the average, below the value expected for uniform straining of the matrix without fibers. The stress points still appear in the same general pattern seen in Fig. 10a, only now there is scatter in the results. An insignificant number of stress points appear below the x-axis due to discretization effects. Matrix shrinkage is restrained local to the steel fibers and fiber clusters so that the matrix strain is no longer uniform (in contrast to the artificial conditions used to produce Fig. 10a).

For the case of non-uniform drying, the data points exhibit additional scatter relative to the data points for uniform drying. Fibers near the surface, where drying shrinkage is most pronounced, experience higher axial compression compared to fibers more centered within the domain. Scatter is greater at earlier ages when the differences in moisture content between the near-surface and interior regions of the specimen are greater. The data points shown in Fig. 10b are for a drying period of $t=10$ days. For longer time periods, the amount of scatter in stress values for the non-uniform drying case diminishes and approaches that of the uniform drying case. For the small specimen studied here, the material achieves near hygral equilibrium with the environment by the end of the simulation period of $t=600$ days (i.e. the diffusion analysis indicates nodal humidities to be in the range $0.5 \le H < 0.54$). Therefore, the diffusion analysis provides almost the same fiber stress patterns in the end as the uniform shrinkage analysis, since the final sum of the ΔH values is nearly the same for all points (even though the ΔH history for each nodal point in the domain is generally different.) If the structural component is large, or if it is subjected to frequent wetting and drying cycles, it will not achieve hygral equilibrium and the scatter in stress values will remain larger for the non-uniform shrinkage analysis. Cracking of the matrix would also cause the stress profiles for the uniform and non-uniform shrinkage cases to be different. The fracture properties of FRCC are affected by non-uniformities in the fiber distribution [34] and, with further development, this modeling approach could be used to study such phenomena.

4.4. Effects of fiber distribution and orientation

Production processes generally affect the distribution of fibers within FRCC components. The specimen cross-section also constrains the range of fiber orientations when the midpoint of the fiber is within $l_f/2$ from one or more of the boundaries. Due to these boundary effects on the fiber distribution, the numerical model exhibits slightly less shrinkage than is predicted by the analytical model of the fiber composite based on a random fiber distribution. However, in the random process for positioning fibers within the domain, fibers extending outside of the domain are rejected whereas fibers completely inside the domain are immediately accepted. The procedure does not account for the dynamics of the consolidation process, in which fibers become directionally aligned with the specimen surfaces as the cement-based material is placed and consolidated. Likewise, the procedure does not account for settlement of the fibers that would cause further alignment with the specimen boundaries. These aspects of the synthetic fiber distribution are partial causes of the apparent reduced efficiency of fibers in the numerical model, relative to that in the experiment. Stroeven [35] has developed methods for generating material structure that include the dynamics of the consolidation process. Alternatively, the actual distribution of fibers and other material structure can be determined through X-ray imaging [36] or serial sectioning followed by stereological reconstruction [37], and then used as input to the numerical model.

For comparison, the same shrinkage simulations are done for the case where all fibers are aligned with the longitudinal axis of the specimen (Fig. 8). The simulated shrinkage strains agree well with those of the analytical model, both of which could be viewed as providing a lower bound solution to the shrinkage strain, since any nonalignment (as would have occurred in the experiment) reduces the amount of restraint in the longitudinal direction in which strains have been measured.

It should be noted that the effects of fiber distribution and orientation also manifest themselves during the fracture of FRCC. This has been observed in numerical simulations using this approach in two dimensions, in which several FRCC panels were loaded in uniaxial tension [31]. The modeling of the panels was identical except for the differing random placement of fibers within the material domain. Since the presence of fibers affects matrix stress prior to cracking, different random placements of fibers lead to different cracking locations. As the fibers are explicitly represented, the model accounts for the

embedded lengths of each fiber and the number of fibers crossing each crack. These factors directly influence the transfer of load across cracks [31] and therefore are important considerations when designing FRCC to achieve pseudo strain hardening, as has been done with high performance fiber reinforced cement composites (HPFRCC) [4,38].

5. Conclusions

In this paper, a novel simulation framework is used to study the pre-cracking restraint provided by fibers during uniform and non-uniform drying of a cement composite. The fibers exist as discrete entities within a three-dimensional, irregular lattice representation of the material matrix. The simulation results are verified using a micromechanical model and through comparisons with experimental data. The paper conclusions are as follows:

1. The presence of stiff fibers serves to reduce overall drying shrinkage of the cement composite, although the degree of shrinkage reduction is not great for the low volume fraction of fibers considered in this work. It is noteworthy that this simple result can be derived from a modeling of each individual fiber in the composite.
2. The model provides insight into the interactions between individual fibers and the matrix during drying shrinkage. For both uniform and non-uniform drying processes, variations in local restraint conditions and fiber group effects produce variations in the axial stresses carried in the individual fibers. Although the fiber axial stress profiles exhibit much scatter, the basic theoretical shape is retained when viewing the collection of stress points as a whole. There are additional differences in the behavior of individual fibers when considering non-uniform drying conditions. Closer to the specimen surface, where drying and therefore shrinkage strains are generally more pronounced, fibers experience higher axial compressive stresses relative to those in the specimen interior.
3. Material parameters for the nonlinear diffusion analyses were back-calculated to give practically the same global shrinkage curve as that of uniform shrinkage according to a prescribed code-type relation. After fibers are added, the two approaches (uniform and non-uniform shrinkage) produce nearly the same effective shrinkage strains over the specimen length. The occurrence of cracking would likely change this scenario.
4. If a FRCC component initially has uniform internal humidity and then approaches hygral equilibrium with the environment over time, the variations in fiber axial stresses due to non-uniform drying diminish and approach those of uniform drying. This is because shrinkage strain increments are based on the change of relative humidity, ΔH, over a time step according to Eq. (10). At hygral equilibrium, the sum of the ΔH at each node would be the same, even though the nodal histories of ΔH are generally different. Material nonlinearity, such as cracking, would likely cause differences in the fiber stresses.

In this work, the lattice approach accounts for the elastic interactions of the individual fibers within a homogeneous matrix, the drying of which is modeled as a process of nonlinear diffusion. To obtain more general results, the effects of other important factors (e.g. concrete heterogeneity, fracture, creep, and other forms of shrinkage) should be present within the analyses. Moreover, fibers are added primarily to restrict crack opening after matrix fracture and their restraining effects prior to cracking, though generally beneficial, are of secondary importance. Nonetheless, the presence of fibers is likely to affect the location of crack initiation and a realistic modeling of the fiber distribution would help to provide insight into how fracture evolves. The two-dimensional fracture simulation presented in Ref. [31] illustrates these considerations. The explicit modeling of fibers, and their realistic distribution within the material, allows for a better understanding of the individual and collective effects of fibers on composite behavior. The case of non-uniform shrinkage serves as a realistic basis for simulating drying shrinkage cracking, whereas the assumption of uniform shrinkage is clearly inappropriate when studying fracture evolution in three-dimensional structures.

Acknowledgement

This work was supported by a US NSF grant (CMS-0201590) to the University of California, Davis. The authors thank Dr. Mien Yip for his valuable contributions to this work.

References

[1] Comite Euro-International du Beton (CEB), Durable Concrete Structures —Design Guide, Thomas Telford Ltd., London, 1992.
[2] P. Balaguru, S.P. Shah, Fiber Reinforced Cement Composites, McGraw-Hill, New York, 1992.
[3] V.C. Li, H. Horii, P. Kabele, T. Kanda, Y.M. Lim, Repair and retrofit with engineered cementitious composites, Eng. Fract. Mech. 65 (2–3) (2000) 317–334.
[4] A.E. Naaman, H.W. Reinhardt (Eds.), High Performance Fiber Reinforced Cement Composites 2 (HPFRCC 2), RILEM Proceedings, vol. 31, E&FN Spon, London, 1995, 502 pp.
[5] M.D. Cohen, J. Olek, W.L. Dolch, Mechanism of plastic shrinkage cracking in Portland cement and Portland cement–silica fume paste and mortar, Cem. Concr. Res. 20 (1) (1990) 103–119.
[6] N. Banthia, C. Yan, Shrinkage cracking in polyolefin fiber-reinforced concrete, ACI Mater. J. 97 (4) (2000) 432–437.
[7] K. Wang, S.P. Shah, P. Phuaksuk, Plastic shrinkage cracking in concrete materials—influence of fly ash and fibers, ACI Mater. J. 98 (6) (2001) 458–464.
[8] R.N. Swamy, H. Stavrides, Influence of fiber reinforcement on restrained shrinkage and cracking, ACI J. (1979) 443–460.
[9] P.S. Mangat, M.M. Azari, Shrinkage of steel fiber reinforced cement composites, Mat. Struct. 21 (1988) 163–171.
[10] J.E. Bolander, S. Saito, Discrete modeling of short-fiber reinforcement in cementitious composites, Adv. Cem. Based Mater. 6 (1997) 76–86.
[11] A. van Hauwaert, J.G.M. van Mier, Computational modeling of the fibre–matrix bond in steel fibre reinforced concrete, in: H. Mihashi, K. Rokugo (Eds.), Fracture Mechanics of Concrete Structures, Aedificatio Publishers, Freiburg, Germany, 1998, pp. 561–571.
[12] J.P.B. Leite, V. Slowik, H. Mihashi, Computer simulation of fracture processes of concrete using mesolevel models of lattice structures, Cem. Concr. Res. 34 (6) (2004) 1025–1033.

[13] E. Schlangen, E.J. Garboczi, Fracture simulations of concrete using lattice models: computational aspects, Eng. Fract. Mech. 57 (2/3) (1997) 319–332.
[14] H. Sadouki, J.G.M. van Mier, Analysis of hygral induced crack growth in multiphase materials, Heron 41 (4) (1996) 267–286.
[15] G. Lilliu, J.G.M. van Mier, 3-D lattice type fracture model for concrete, Eng. Fract. Mech. 70 (2003) 927–941.
[16] G. Cusatis, Z.P. Bažant, L. Cedolin, Confinement-shear lattice model for concrete damage in tension and compression: I. Theory, J. Eng. Mech. 129 (12) (2003) 1439–1458.
[17] A. Okabe, B. Boots, K. Sugihara, Spatial tessellations: concepts and applications of Voronoi diagrams, Wiley Series in Probability and Mathematical Statistics, John Wiley and Sons Ltd, England, 1992.
[18] Z.P. Bazant, L.J. Najjar, Drying of concrete as a nonlinear diffusion problem, Cem. Concr. Res. 1 (1971) 461–473.
[19] G. Martinola, F.H. Wittmann, Application of fracture mechanics to optimize repair mortar systems, in: F.H. Wittmann (Ed.), Fracture Mechanics of Concrete Structures, Aedificatio Publishers, Freiburg, 1995, pp. 1481–1486.
[20] R.W. Lewis, K. Morgan, H.R. Thomas, K.N. Seetharamu, The Finite Element Method in Heat Transfer Analysis, John Wiley and Sons, Chichester, UK, 1996.
[21] T.J.R. Hughes, The Finite Element Method—Linear Static and Dynamic Finite Element Analysis, Prentice-Hall, Inc., Englewood Cliffs, NJ, 1987, 803 pp.
[22] J. Marchand, B. Gérard, New developments in the modeling of mass transport processes in cement-based composites—a review, Advances in Concrete Technology—Proceedings Second International CANMET/ACI International Symposium (SP-154), ACI, 1995, pp. 169–210.
[23] J. Kropp, H.K. Hilsdorf, H. Grube, C. Andrade, L.-O. Nilsson, Transport mechanisms and definitions, in: J. Kropp, H.K. Hilsdorf (Eds.), Performance Criteria for Concrete Durability, RILEM Report, vol. 12, 1995, pp. 4–14.
[24] J.E. Bolander, S. Berton, Simulation of shrinkage induced cracking in cement composite overlays, Cem. Concr. Compos. 26 (2004) 861–871.
[25] FEMLAB v2.3, COMSOL AB, Stockholm, Sweden, 2002.
[26] T. Kawai, New discrete models and their application to seismic response analysis of structures, Nucl. Eng. Des. 48 (1978) 207–229.
[27] S. Berton, J.E. Bolander, Crack band modeling of fracture in irregular lattices, Journal of Computer Methods in Applied Mechanics and Engineering (in press).
[28] M. Yip, J. Mohle, J.E. Bolander, Automated modeling of 3-D structural components using irregular lattices, Comput.-Aided Civil Infrastruct. Eng. 20 (6) (2005) 393–407.
[29] H.L. Cox, The elasticity and strength of paper and other fibrous materials, Br. J. Appl. Phys. 3 (1952) 72–79.
[30] A. Bentur, S. Mindess, Fiber Reinforced Cementitious Composites, Elsevier Science Publishers, Ltd., London, 1990.
[31] J.E. Bolander, N. Sukumar, Irregular lattice model for quasistatic crack propagation, Phys. Rev., B 71 (094106) (2005) (12 pp.).
[32] M. Yip, Z. Li, B.-S. Liao, J.E. Bolander, Irregular lattice models of fracture of multiphase particulate materials, International J. Fracture (in press).
[33] J. Zhang, V.C. Li, Influences of fibers on drying shrinkage of fiber-reinforced cementitious composite, ASCE J. Eng. Mech. 127 (1) (2001) 37–44.
[34] Y. Akkaya, S.P. Shah, B. Ankenman, Effect of fiber dispersion on multiple cracking of cement composites, ASCE J. Eng. Mech. 127 (4) (2001) 311–316.
[35] M. Stroeven, Discrete Numerical Modelling of Composite Materials, PhD degree thesis, Delft University of Technology, The Netherlands, 1999.
[36] P. Stroeven, S.P. Shah, Use of radiography-image analysis for steel fibre reinforced concrete, in: R.N. Swamy (Ed.), RILEM Symposium 1978: Testing and Test Methods for Fibre Cement Composites, The Construction Press, UK, 1978, pp. 275–288.
[37] J.E. Bolander, M.A. Perez Lara, Modeling fiber distribution effects within cement composites, in: M.A. Mansur, K.C.G. Ong (Eds.), Seventh International Symposium on Ferrocement and Thin Reinforced Cement Composites, National University of Singapore, Singapore, 2001, pp. 131–142.
[38] V.C. Li, From micromechanics to structural engineering—the design of cementitious composites for civil engineering applications, J. Struct. Mech. Earthquake Eng. 10 (2) (1993) 37–48.